



Seismicity and state of stress in the central and southern Peruvian flat slab



Abhash Kumar^{a,*}, Lara S. Wagner^b, Susan L. Beck^c, Maureen D. Long^d, George Zandt^c, Bissett Young^{a,1}, Hernando Tavera^e, Estella Minaya^f

^a Department of Geological Sciences, University of North Carolina at Chapel Hill, 104 South Rd., Mitchell Hall, CB #3315, Chapel Hill, NC 27599-3315, USA

^b Department of Terrestrial Magnetism, Carnegie Institution for Science, 5241 Broad Branch Road, NW, Washington, DC 20015-1305, USA

^c Department of Geosciences, University of Arizona, 1040 E. 4th Street, Tucson, AZ 85721, USA

^d Department of Geology and Geophysics, Yale University, 210 Whitney Avenue, New Haven, CT 06511, USA

^e Instituto Geofísico del Perú, Calle Badajo No. 169, Urb. Mayorazgo IV Etapa, Lima, Peru

^f El Observatorio San Calixto, Calle Indaburo 944, Casilla 12656, La Paz, Bolivia

ARTICLE INFO

Article history:

Received 5 August 2015

Received in revised form 9 February 2016

Accepted 11 February 2016

Editor: P. Shearer

Keywords:

Nazca plate

Peru

ridge buoyancy

subduction geometry

flat slab

ABSTRACT

We have determined the Wadati–Benioff Zone seismicity and state of stress of the subducting Nazca slab beneath central and southern Peru using data from three recently deployed local seismic networks. Our relocated hypocenters are consistent with a flat slab geometry that is shallowest near the Nazca Ridge, and changes from steep to normal without tearing to the south. These locations also indicate numerous abrupt along-strike changes in seismicity, most notably an absence of seismicity along the projected location of subducting Nazca Ridge. This stands in stark contrast to the very high seismicity observed along the Juan Fernandez ridge beneath central Chile where, a similar flat slab geometry is observed. We interpret this as indicative of an absence of water in the mantle beneath the overthickened crust of the Nazca Ridge. This may provide important new constraints on the conditions required to produce intermediate depth seismicity. Our focal mechanisms and stress tensor inversions indicate dominantly down-dip extension, consistent with slab pull, with minor variations that are likely due to the variable slab geometry and stress from adjacent regions. We observe significantly greater variability in the P-axis orientations and maximum compressive stress directions. The along strike change in the orientation of maximum compressive stress is likely related to slab bending and unbending south of the Nazca Ridge.

© 2016 Elsevier B.V. All rights reserved.

1. Introduction

The term “flat slab subduction” is often used to refer to the subduction of an oceanic plate that enters the trench at a normal dip angle ($\sim 30^\circ$), continues subduction up to 100 km depth, and then abruptly bends to travel horizontally ($\sim 0^\circ$ dip) for several hundred kilometers before resuming its descent (Hasegawa and Sacks, 1981; Cahill and Isacks, 1992). The depth of flattening and inboard extent of the horizontal segment varies between different regions of flat slab subduction, for reasons that are still under investigation (e.g. Manea and Gurnis, 2007; Gerya et al., 2009; Manea et al., 2011; Hu et al., 2016). Flat slab subduction is of particular interest because it has often been causally linked to unusual tectonic processes such as the cessation of arc volcanism, inboard thick-

skinned deformation of the overriding plate and the evolution of high plateaus (e.g. Isacks and Barazangi, 1977; Jordan and Allmendinger, 1986). In particular, the Laramide uplift of the Rocky Mountains and subsequent ignimbrite flare-up in the western United States have been attributed to a period of flat subduction of the Farallon plate (80–55 Ma) (e.g. Dickinson and Snyder, 1978; Humphreys et al., 2003).

In this study, we investigate the southern portion of the Peruvian flat slab (Fig. 1). The western margin of Peru between 2° and 15° S is characterized by the flat subduction of the oceanic Nazca plate beneath the continental South American plate (e.g. Hasegawa and Sacks, 1981; Cahill and Isacks, 1992; Hayes et al., 2012; Dougherty and Clayton, 2014). The Peruvian flat slab is associated with the marked absence of any known Quaternary arc volcanism and with generally low surface heat flow measurements (Henry and Pollack, 1988). While the causes of flat slab subduction are still controversial (e.g. Gerya et al., 2009; Skinner and Clayton, 2013), one possible contributing factor beneath Peru is the subduction of the less dense oceanic lithosphere associated with

* Corresponding author.

E-mail address: abhash.kumar84@gmail.com (A. Kumar).

¹ Now at Donskoj and CO, Kingston, NY.

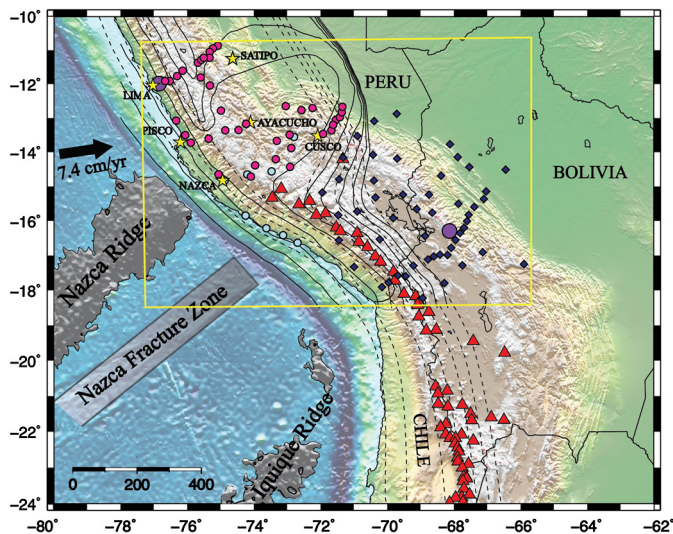


Fig. 1. Map showing the Peruvian flat slab region, our study area (yellow box), and the locations of seismic stations used in this study. Dark pink circles are PULSE stations. Dark blue diamonds are CAUGHT stations and light blue circles are PERUSE stations used in this study. Large purple circles represent GSN stations at Lima, Peru and La Paz, Bolivia. Yellow stars are the location of important cities. Red triangles are Holocene volcanoes (INGEMMET, www.ingemmet.gob.pe). Solid lines are slab contours from Antonijevic et al. (2015). Dashed lines are slab contours from Cahill and Isacks (1992). The Nazca Ridge, Iquique Ridge and Nazca Fracture Zone are shaded gray offshore. The black arrow offshore represents the plate motion of the Nazca plate from HS3-NUVEL1A (Gripp and Gordon, 2002). (For interpretation of the references to color in this figure legend, the reader is referred to the web version of this article.)

the Nazca Ridge (e.g. Hu et al., 2016). The crust of the Nazca Ridge is unusually thick (~ 17 km) and was formed at the Pacific Nazca spreading center along with its conjugate on the Pacific Plate, the Tuamotu Plateau, in the early Cenozoic (Hampel, 2002; Hampel et al., 2004). The track of the Nazca Ridge and the convergence direction are not parallel (Fig. 1), resulting in a southward migration of the ridge relative to the overriding continent. Since it first began subducting ~ 11.2 Ma at $\sim 11^\circ$ S (Hampel, 2002), the ridge has migrated ~ 480 km south relative to the South American margin (Hampel, 2002; Hampel et al., 2004). The timing of slab flattening is well constrained by radiometric ages of the cessation of arc volcanism, episodes of intense metallogenic activity (Rosenbaum et al., 2005) and basement involved thrust deformation (Shira uplift) on the overriding South American plate. The spatio-temporal pattern of these indicators seems to follow the southward migration of the Nazca Ridge (Rosenbaum et al., 2005; Bissig et al., 2008).

Previous studies have analyzed the Wadati–Benioff zone (WBZ) seismicity in Peru, primarily using data from stations at teleseismic distances or local data collected from small seismic networks (Hasegawa and Sacks, 1981; Cahill and Isacks, 1992; Hayes et al., 2012). Here we present estimates of earthquake locations and focal mechanisms for slab events between 10° and 18.5° S using data from three co-deployed local seismic networks. We also estimate the regional stress field tensor south of the Nazca Ridge in order to better understand the current state of stress of the subducting slab in this region of complex subduction geometry. We note a number of striking seismicity patterns that may indicate variations in slab hydration and dehydration processes along strike. Our regional stress field estimates show significant changes over short spatial scales, consistent with the rapidly changing slab geometry. For the most part, our results are consistent with previous work showing down-dip extension below 60 km depth (Marot et al., 2013; Rontogianni et al., 2011), with slight variations likely due to the regional tectonic setting and complex slab geometry.

2. Data

We use data collected from the temporary broadband stations of three independent seismic arrays (Fig. 1). The CAUGHT (Central Andean Uplifts and the Geodynamics of High Topography) experiment comprised 50 broadband seismometers deployed for 21 months between November 2010 and July 2012 between 13° S to 18° S across the northern Altiplano. Thirty stations were deployed in Bolivia and 20 stations in Peru with a higher density line across the cordillera that spanned both Peru and Bolivia. The “PULSE” (PerU Lithosphere and Slab Experiment) network (e.g., Antonijevic et al., 2015) was deployed from May 2011 to June 2013 and consisted of 40 broadband seismometers. The PULSE network was located above the southern part of the Peruvian flat slab roughly along three transects. The southern transect extended north and east from the city of Nazca to beyond Cusco. The middle and northern transects were located between Pisco and Ayacucho, and Lima and Satipo, respectively. The northern transect was situated above the paleo-location of the subducted Nazca Ridge between 10–8 Ma (Rosenbaum et al., 2005). The southern and middle transects straddle the projected current location of the subducted Nazca Ridge. We also use data from the PERUSE project deployed by the California Institute of Technology and UCLA between July 2008 and June 2012 (e.g., Phillips and Clayton, 2014). We use data for 8 stations from this deployment located along the coast in southern Peru and along the southern transect of the PULSE network.

3. Methods

3.1. Event locations and error analyses

We identify possible earthquakes recorded by our three arrays using the dbdetect tool that is part of the ANTELOPE software package (<http://www.brrt.com>). This method is based on a short-term average (STA) versus long-term average (LTA) trigger mechanism. An event is detected if the ratio of energy between STA and LTA windows exceeds a user-defined threshold. We use an energy threshold ratio of 5 and STA and LTA moving time windows of 1 second and 10 seconds respectively. Of the 3000 possible events identified, we selected 952 earthquakes after individual inspection of the seismic waveforms for each event.

We calculate absolute event hypocenter locations using the single event location algorithm HYP, incorporated into the SEISAN software package (Havskov and Ottemoller, 1999). HYP determines earthquake locations using an iterative linearized least squares inversion of travel time data (Aki and Lee, 1976). We use a modified version of the P-wave velocity model of Dorbath and Granet (1996) that takes into account the 65 km average crustal thickness in our study area as determined from recent analyses of teleseismic receiver functions (Phillips and Clayton, 2014; Bishop et al., 2014). S-wave velocities are determined using a V_p/V_s ratio of 1.75 (Dorbath and Granet, 1996).

In order to determine the sensitivity of our event locations to starting depth, we calculate the hypocenters of all 952 events with a starting depth of 5 km, 100 km, 200 km, and the initial hypocentral depth from dbdetect. Of the 952 events, 838 had final depths that differ by less than 10 km irrespective of the starting depths. From those 838 events, we then select events with depths greater than 50 km and azimuthal gaps $< 270^\circ$. For events south of 15° S, we eliminated those events with depth errors of > 15 km. Given the sparsity of seismicity north of 15° S, we included some events with slightly larger depth errors whose latitudes, longitudes, and depths were stable over all tested starting depths. After these criteria were applied, we are left with 568 event locations.

We add to this list by investigating those 114 events where the range of event depths determined with different starting depths was >10 km. We divide this list of 114 events into two sets depending on the number of similar depths recovered from our four starting depths. The first set of events includes 45 earthquakes for which three of the four original hypocentral locations differ in depth by less than 10 km. We calculate travel time residuals corresponding to each of the three starting depths and select the location with the minimum travel time residual as our preferred hypocenter. If travel time residuals are the same for more than one starting depth then the location whose starting depth is closest to the hypocentral depth is selected. We recalculate event locations for each event in the first set using their best starting depth and obtain 16 robust event locations following the same cutoff criteria as used previously (depth >50 km, azimuthal gap $<270^\circ$, with less than 15 km error in depth).

The second subset of events includes 68 earthquakes for which the hypocenters corresponding to the four starting depths (5 km, 100 km, 200 km and the initial hypocentral depth from dbdetect) have two or fewer final depths that are within 10 km of each other. We test several other starting depths at 25 km intervals for each of these events and calculate travel time residuals corresponding to each starting depth. We look for at least 3 similar depths (<10 km difference) recovered from inversions with three adjacent starting depths, and travel time residuals of less than 3 seconds. Using these criteria, we obtain hypocentral locations for 36 events. We recalculate event locations for each event using their best starting depths and obtain 7 event locations that satisfied the additional aforementioned cutoff criteria (depth >50 km, azimuthal gap $<270^\circ$, with less than 15 km error in depth). We finally add these 23 robust event locations (16 from the first group and 7 from the second) to the 568 events described earlier for a total of 591 robust event hypocenters (Fig. 2a; see Supplemental Table T1). South of the Nazca Ridge the error in event depth is small and varies between 2.6–14.9 km. North of the Nazca Ridge, depth error varies between 2.3–25 km, with 10 more events having depth error in the range of 25–32.4 km.

We test the sensitivity of our event hypocenters to velocity models by subtracting and adding 5% to both the P and S wave velocities of each layer in our velocity model. The results of these tests are shown in Figs. 3a and b. The average depth for the fast model is 0.86 km deeper than our preferred model, and the average depth for the slow model is 0.79 km shallower than our preferred model. The average spread in the depths of hypocenters for a given event between velocity models is 7 km with a standard deviation of 6 km. The most significant differences are seen for the deepest events with the longest travel paths, as expected. While individual events have slight differences in depth depending on the velocity model used, the overall patterns observed remain robust.

We relocate our 591 events using the double difference technique of Waldhauser and Ellsworth (2000). This method takes advantage of the nearly identical ray paths of two nearby events recorded at a common station. HypoDD uses both absolute and relative travel time data for each pair of events to determine relative event locations that are independent of regional structural variations. We calculate differential times between common phases recorded at a common station for all events pairs separated by ≤ 40 km. Each event is grouped to a maximum of 10 neighboring events with inter-event distances ≤ 40 km, each of which were required to have at least eight differential travel time observations. Of the 591 events located using HYP, we were able to relocate 508 events with HypoDD (Fig. 2b; Supplemental Table T2). The remaining 83 events did not have sufficient neighboring earthquakes at small inter-event distances (≤ 40 km) for a stable relative relocation.

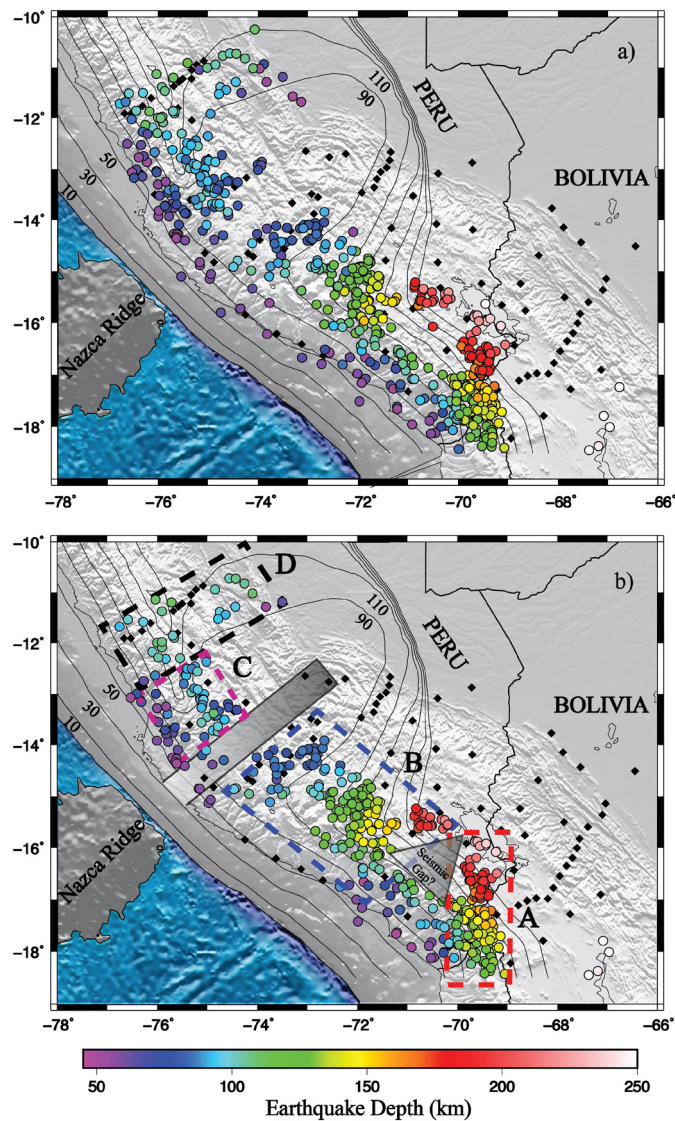


Fig. 2. Earthquake hypocenters calculated using (a) single event location method (b) relative relocation method. The hypocenters are color coded by depth. Black diamonds are the stations used in the location process. Solid lines are slab contours from Antonijevic et al. (2015). Dashed boxes outline the regions of various clusters (A–D) of events identified in the study area. Shaded triangle represents the seismic gap between cluster A and B at depth ≤ 120 km. Note the absence of seismicity (shaded rectangle) along the projected location of the subducting Nazca Ridge.

3.2. Focal mechanisms and stress tensor calculation

We determine the best fitting double-couple fault plane solution and associated P and T axis orientations using FPFIT (Reasenber and Oppenheimer, 1985), included in the software package SEISAN (Havskov and Ottemoller, 1999). It estimates source model parameters (strike, dip and rake) through a grid search by iteratively minimizing the weighted sum of first motion polarity errors (Fig. 4). We perform an initial grid search at coarse increments of 20° in strike, dip and rake and then used a finer grid of 1° increments to determine the best fitting solution. We use the error estimation procedure of FPFIT to calculate the error in strike, dip, and rake of the focal mechanism solutions. FPFIT calculates the standard deviation misfit function between the observed and predicted polarity of each station and estimates the variance in this misfit function from a priori knowledge (quality of phase pick) of the variance in the observed data. The 90-percent confidence interval for the misfit function is estimated from its

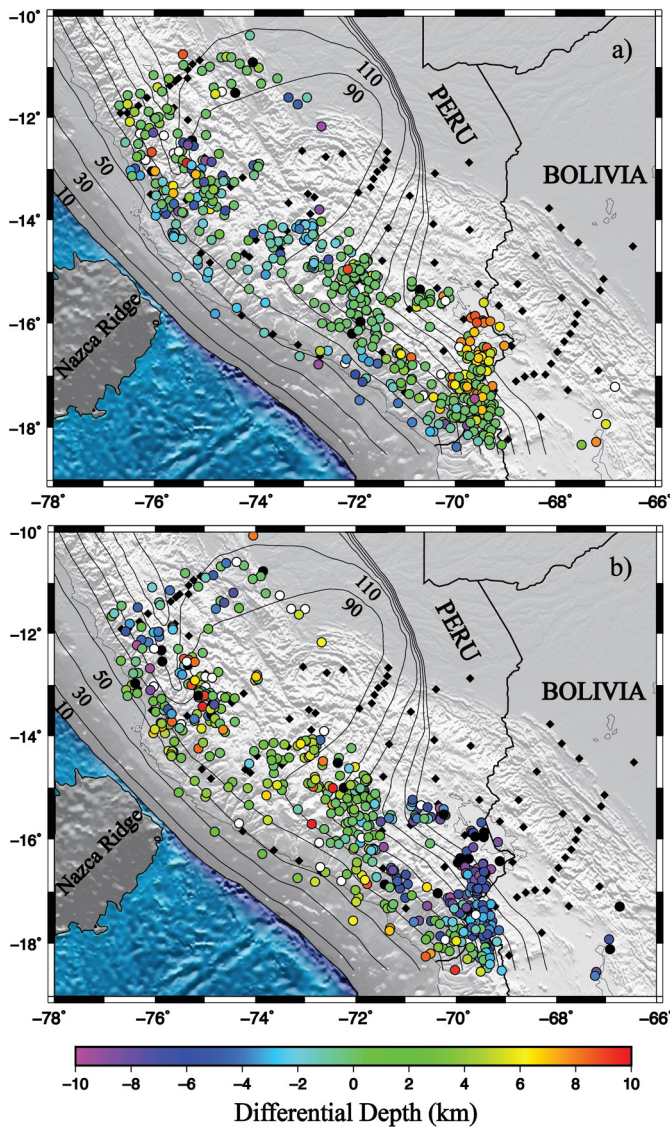


Fig. 3. Earthquake hypocenters calculated using single event location method (a) by subtracting 5% (b) by adding 5% to our velocity model. The hypocenters are color coded by calculating the difference between hypocentral depth for our velocity model and the modified (slow and fast) velocity model. Events with cool colors (left half of the color scale) represent downward shifted events and events shown in warm colors (right half of the color scale) are upward shifted events. Black diamonds are the stations used in the location process. Solid lines are slab contours from Antonijevic et al. (2015).

variance by assuming that the misfit is normally distributed. The error in each model parameter (e.g. strike, dip, and rake) is determined with respect to the minimum misfit value (Reasenber and Oppenheimer, 1985). We do not include solutions with sparse polarity readings and those for which all readings are close to nodal planes in further analyses. Additionally, we use the following criteria to select the best available focal mechanism solutions: at least 10 polarity readings, a maximum of 2 incorrect polarities and a maximum 10° error in strike and dip and 20° error in rake. This produces a total of 173 robust focal mechanism solutions.

We use our observed focal mechanisms, including strike and dip of the fault plane and the sense of relative motion (rake) along those faults, to calculate the regional stress field tensor (Delvaux and Sperner, 2003). The stress tensor inversion minimizes the angular misfit between the observed and predicted slip directions. To calculate the error on strike and dip of stress axes (σ_1 , σ_2 , σ_3), the inversion algorithm test wide range of orientations of the three

stress axes by performing a series of rotation, successively around sigma 1, sigma 2, and sigma 3 axes (Delvaux and Sperner, 2003). It finds the range of rotation angle for which the value of angular deviation between the observed and theoretical slip is less than user defined threshold. The error on strike and dip of the stress axes is therefore related to the angular aperture (range of rotation angle) of a cone centered on the stress axes.

Given the likelihood that the state of stress in the subducting plate varies depending on the changing slab geometry, we perform independent stress analyses on four sub-regions south of the Nazca Ridge that comprise areas with consistent slab dip angles inside Box 1, 2 (2S and 2N), and 3, south of the Nazca Ridge (black rectangles, Fig. 8) and calculate the regional stress field for each subregion individually. We do not include the area north of the Nazca Ridge for stress tensor inversion due to the sparsity of focal mechanism observations and complex slab geometry (Antonijevic et al., 2015). In Box 1, we choose the central portion for stress tensor inversion, where the slab dip is constant. We exclude the southernmost portion of Box 1, where the direction of slab dip is different than the majority of T-axes measurements in the central portion of Box 1. In Box 2, the slab dip direction varies from NE in the south to SE in the north (Fig. 8). We choose two small subregions 2S and 2N in Box 2 for stress inversions, one that lies south of the bend and one to the north of the bend (Fig. 8). In Box 3, the slight downdip direction of nearly horizontal slab is directed towards SE and we selected all the events with known focal mechanism for stress calculation in Box 3 (Fig. 8).

4. Results

4.1. Earthquake locations

The results of our single event locations and relative relocations are shown in Figs. 2a and b respectively. A direct comparison of the relative and absolute locations is shown in Fig. S1. Cross sections of our relative relocations are shown in Fig. 5 and in Figs. S2 and S3 of the supplementary material. We observe a number of distinctive patterns across our study area, including regions of dense seismic activity, regions with sparse seismicity, and some regions in which we were able to find no well-located events.

Our southernmost cluster (labeled “A” in Fig. 2b) comprises a linear, northward trending band of seismicity between 69°W and 70°W. The distinct eastern margin of this cluster is well resolved, and is visible in previous catalogs of seismicity, albeit less clearly. The north–south trend of this cluster does not correspond to the local dip direction of the slab, the convergence direction of the plates, or any known structure within the subducted plate. The seismicity in this region generally defines a slab descending at a constant dip of ~30° (measured orthogonally to the trench) to at least 200 km depth (Figs. 5c and S3 of the supplementary material).

Seismicity is laterally continuous between clusters A and B at depths of <120 km. However, at greater depths we find evidence of a small seismic gap, triangular in shape (shaded triangle, Fig. 2b). This gap is concentrated in the middle of our seismic network, directly beneath one of the CAUGHT stations (CP07), and so is unlikely to be due to a lack of station coverage. We do have an absolute location for one event in the center of this triangle (Fig. 2a), but we are unable to find stable relative locations for that single event due to insufficient neighboring earthquakes. The next cluster to the north (labeled B, Fig. 2b) comprises a large number of events between the northwestern edge of the triangular seismic gap and the southern edge of the projected location of Nazca ridge. Events along the northern edge of this cluster, in the immediate vicinity of the projected location of subducted Nazca Ridge, are the shallowest we have found within the flat slab. There is a

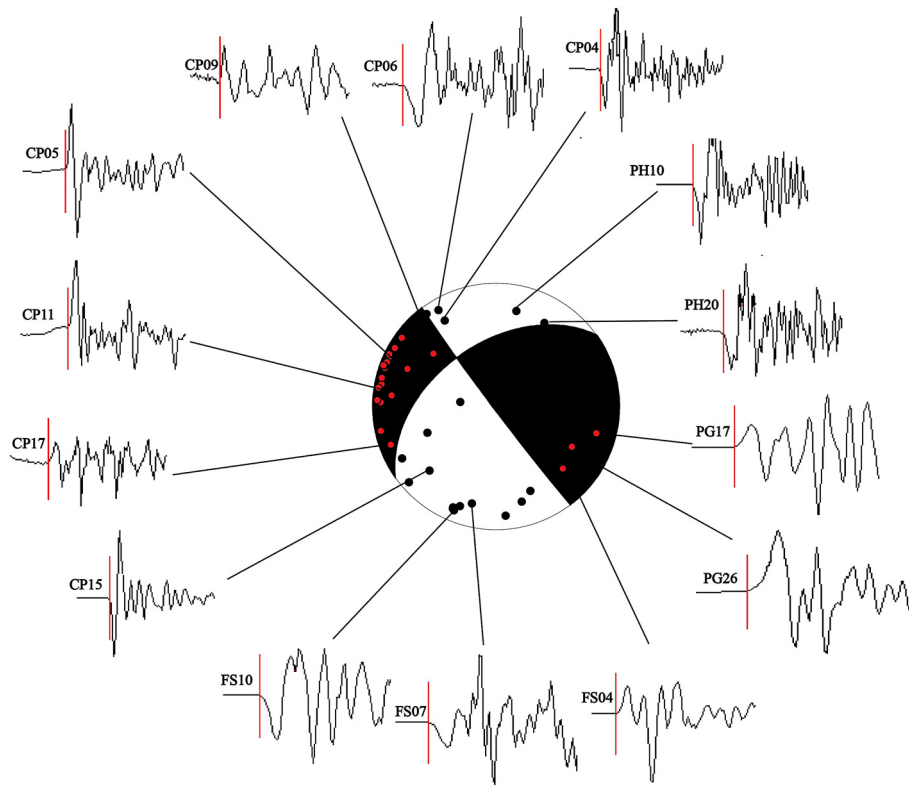


Fig. 4. An example of high-quality focal mechanism solution (lower hemisphere projection) determined from first motion polarity at 37 stations. Red dots indicate compressional (up) arrival and black dots tensional (down) arrival. P-waveform used to determine this solution is shown with marked position of first arrival (red vertical line). (For interpretation of the references to color in this figure legend, the reader is referred to the web version of this article.)

continuous increase in event depths within this cluster both from north to south as well as from west to east, showing a smooth contortion of the slab. Our observed seismicity (cross section CC', Fig. S3) in this contorted region is in good agreement with the previous study of Boyd et al. (1984), who also proposed contortion as opposed to tearing in the slab, where the geometry of subduction changes from flat to normal.

Between clusters B and C, along the projected location of the subducted Nazca ridge, seismicity is anomalously absent at depths below 80 km (shaded rectangle, Fig. 2b; dotted ellipse, Fig. 5b). This observation is distinctly different than the reported seismicity along the Juan Fernandez ridge track in central Chile where seismicity is particularly abundant (Anderson et al., 2007; Hayes et al., 2012). The trench parallel cluster C (Fig. 2b) beneath the Western Cordillera, north of the Nazca ridge, is confined to the westernmost margin of the horizontal portion of the flat slab. This defines its own linear cluster of events, connecting the diffuse seismicity along the northern edge of PULSE network and seismic gap along the projected location of the subducted Nazca ridge. We find very few events inboard of this cluster except for a small number of relatively shallow events with depths between 50 and 70 km for which we are unable to determine relative relocations (Fig. 2a).

Along the northernmost end of our study area, the observed slab seismicity (denoted as cluster D in Fig. 2b) has a maximum inboard extent of over 400 km from the trench. The events in this cluster are generally diffuse and range in depth from ~100 to 120 km, significantly deeper than events found closer to the Nazca Ridge further south.

4.2. Focal mechanisms and stress analyses

Our full focal mechanism solutions are shown in map view in Fig. 6 and in Figs. S4 and S5 of the supplementary material. T-axis

orientations are shown in Fig. 7. The results of our focal mechanism analyses indicate a predominance of normal faulting across our study area (Fig. 6, Table T3 in the supplementary material). In our southernmost region (Box 1, Fig. 7), the T-axes have slightly variable orientations, but are oriented dominantly E–W to ENE–WSW (inset1, Fig. 7). We find that the T-axes are generally parallel to the slab in Box 1, but rotated ~30–40° clockwise from the down-dip direction (black squares, Fig. 9a). Our stress tensor solution shows a similar pattern with the least compressive stress (σ_3 , red arrow in Fig. 9a) oriented parallel to the dipping slab just north of E–W (strike = 83° and dip = 35°, with 1-sigma standard error of 20.4°). The maximum compressive stress (σ_1 , blue arrow in Fig. 9a) is nearly horizontal and oriented N–S.

In Box 2, we see a well-distributed range of T-axis orientations at significantly different azimuths (inset2, Fig. 7). This is to be expected, given the range in slab dip directions in this region. If we focus on the two boxes used to calculate the stress tensors, within which slab orientation is relatively constant (Box 2S and Box 2N, Fig. 8) we see distinct differences between the two. In Box 2S, the T-axes show a generally slab parallel orientation (Fig. 9b). The σ_3 axis is directed ENE at strike = 64° and dip = 12°, with 1-sigma standard error of 17.6°, indicating a slab parallel, down-dip orientation with a similar slight clockwise rotation as is observed in Box 1. However, unlike Box 1, the maximum compressive stress (σ_1) is nearly perpendicular to the slab surface (solid red circle, Fig. 9b). In Box 2N, the T-axes again lie within the slab and are dominantly oriented down-dip (black squares, Fig. 9c). The least compressive stress (σ_3) is also generally parallel to the shallow down-dip direction (red arrow in Fig. 9c). Specifically, σ_3 is oriented ESE with a strike = 114°, dip = 12°, and 1-sigma standard error of 21.1°. The maximum compressive stress (σ_1) is nearly horizontal and oriented parallel to the strike of the slab (blue arrow in Fig. 9c). This

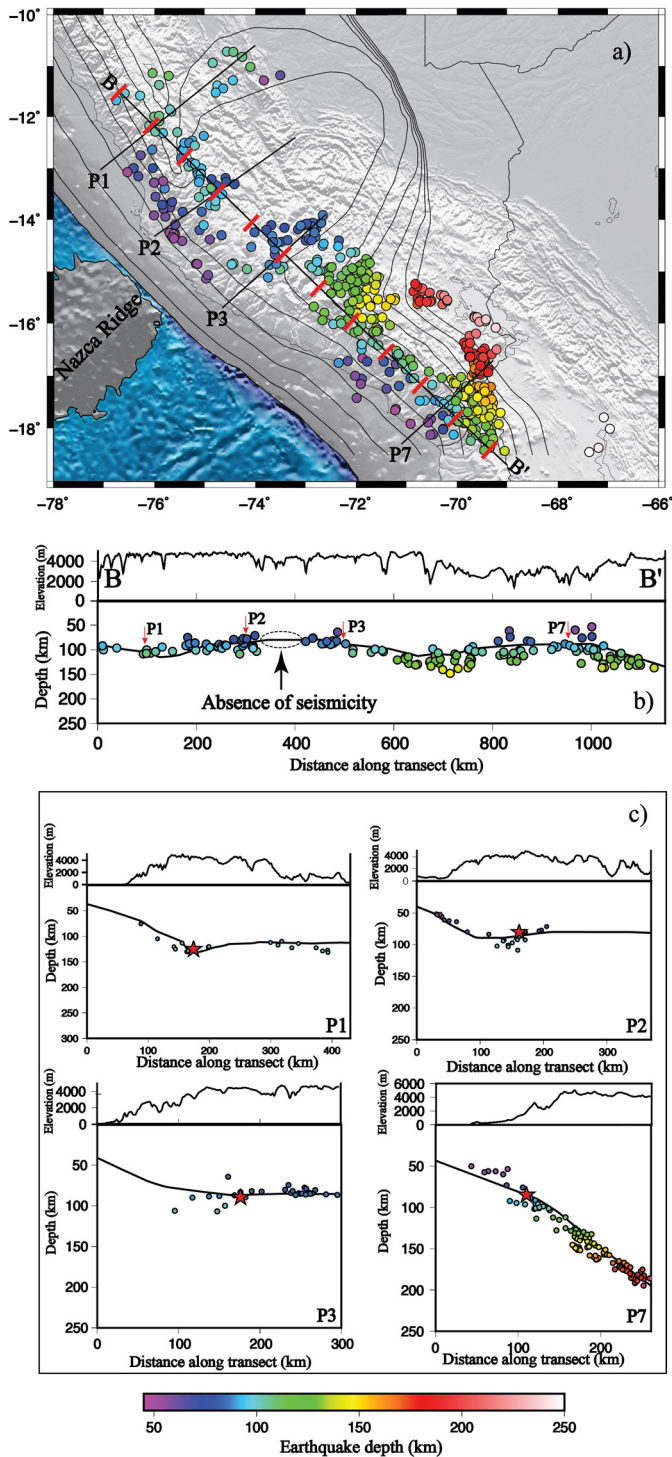


Fig. 5. Map showing locations of (a) trench-parallel (BB') and trench-perpendicular (P1, P2, P3, and P7) transects used to plot seismicity cross-sections. Red tick marks on BB' represents distance interval of 100 km. (b) Seismicity cross-sections BB', parallel to the trench. Dotted ellipse mark the absence of seismicity along the projected location of the subducted Nazca ridge track. Red arrows mark the intersection with trench-perpendicular cross sections. (c) Seismicity cross-sections (P1, P2, P3, and P7) perpendicular to the trench. Earthquakes within ± 35 km are projected onto each cross-section. The solid line in each cross section is the slab contour from Antonijevic et al. (2015). Red star in each trench-perpendicular cross section marks the intersection with BB' cross section. See Figs. S2 and S3 of the supplementary material for the remaining set of trench-parallel and trench-perpendicular seismicity cross-sections. (For interpretation of the references to color in this figure legend, the reader is referred to the web version of this article.)

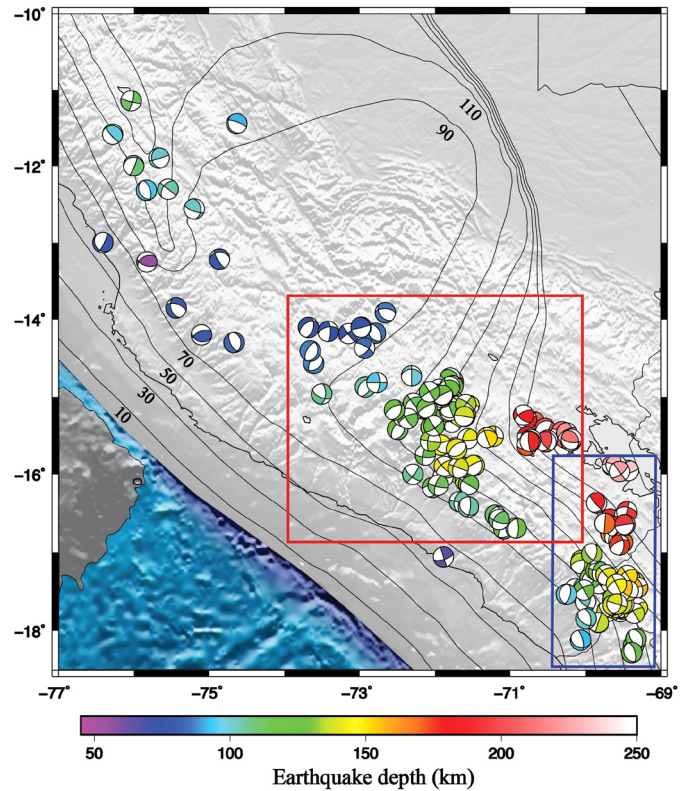


Fig. 6. Map of first motion focal mechanisms plotted in lower hemisphere projection. Mechanisms are color coded by earthquake depth and mainly show normal faulting across the study area. Solid lines are slab contours from Antonijevic et al. (2015). See Figs. S4 and S5 of the supplementary material for zoom-in map of focal mechanism for events inside the red and blue box respectively. (For interpretation of the references to color in this figure legend, the reader is referred to the web version of this article.)

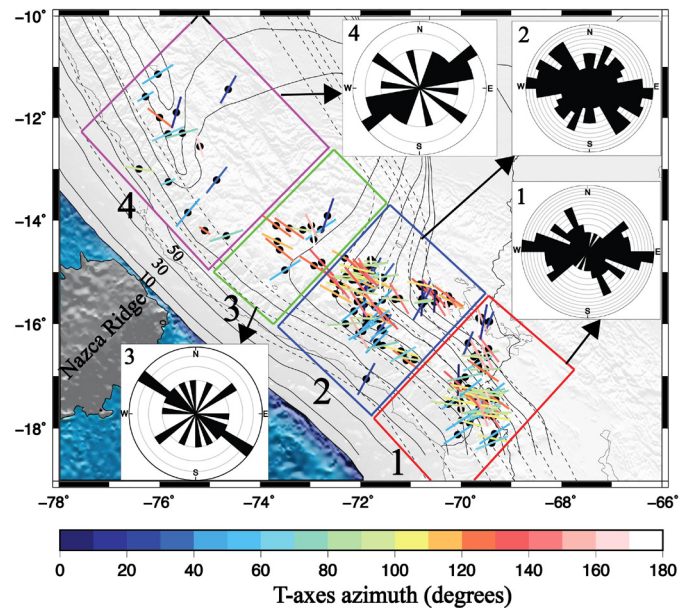


Fig. 7. Map showing T-axes (color sticks) orientations determined from focal mechanism solutions (see Fig. S6 of the supplementary material for P-axis orientations). Length of the T-axis segment is proportional to the dip of T-axes, with smaller segments representing steeper T-axes. Black dots indicate the location of associated slab events. Slab contours (solid black lines) are from Antonijevic et al. (2015). Colored boxes divide the study area into four different regions based on the geometry of subduction. Rose diagrams of the T-axis orientations for each individual box are shown in smaller insets. (For interpretation of the references to color in this figure legend, the reader is referred to the web version of this article.)

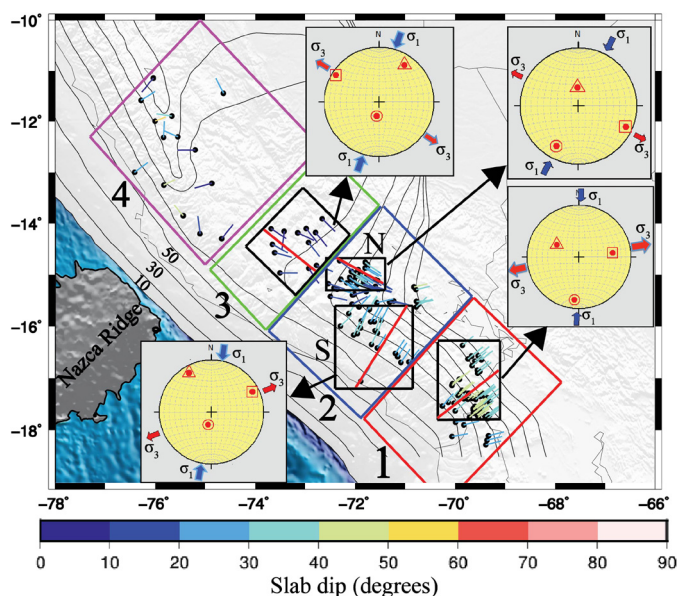


Fig. 8. Map showing the orientations of slab dip vectors (color sticks). Color of the vectors is proportional to the dip of the slab. Slab contours (solid black lines) are from Antonijevic et al. (2015). Colored boxes divide the study area into four different regions, similar as Fig. 7. Black rectangles south of the Nazca Ridge covers the smaller region of constant dip for which stress axes orientations (smaller insets) are determined. A red diagonal line in each black rectangle is the location of cross sections used to compare the T-axes and stress axis in Fig. 10. (For interpretation of the references to color in this figure legend, the reader is referred to the web version of this article.)

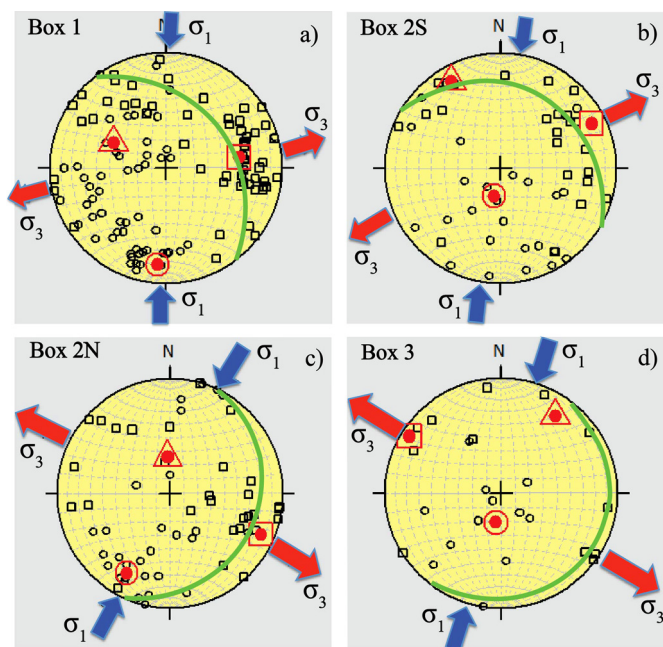


Fig. 9. (a–d) Stress tensor orientations for black rectangular region inside Box 1, 2 (2S and 2N) and 3, respectively, shown in Fig. 8. Red and blue arrows show the azimuth of minimum (σ_3) and maximum (σ_1) compressive stress, respectively. Black circles and squares on each stereonet show the P and T-axes orientations associated with each earthquake, respectively. A great circle (green color) on each stereonet represents the average slab orientation in the region. (For interpretation of the references to color in this figure legend, the reader is referred to the web version of this article.)

is very different to Box 2S where the maximum compressive stress (σ_1) is slab perpendicular.

The flat slab region just south of the Nazca Ridge (Box 3, Figs. 7 and 8) is characterized by comparatively few focal mech-

anisms. The T-axes have variable orientations, all of which are essentially horizontal and nearly parallel to the flat slab surface (black squares, Fig. 9d). The least compressive stress (σ_3) is horizontal and parallel to very slight downdip direction of the slab (red arrow in Fig. 9d). Specifically, σ_3 is directed NW–SE at strike = 301° and dip = 8° , with 1-sigma standard error of 17.4° . The maximum compressive stress (σ_1 , solid red circle in Fig. 9d) and P-axes (black circles, Fig. 9d) are nearly vertical and orthogonal to the slab, similar to Box 2S, but different from the adjacent Box 2N.

In Box 4, north of the Nazca Ridge, the T-axes have variable orientations (Fig. 7). This variable state of stress of the subducting slab is perhaps affected by the presence of proposed tear and complex slab geometry north of the Nazca Ridge (Antonijevic et al., 2015). We do not perform stress tensor inversion in this region due to the likely non-uniformity in the stress field and sparsity of focal mechanism solutions.

5. Discussion

5.1. Abrupt variations in seismicity within the subducted Nazca plate

The earthquake locations presented here show abrupt spatial changes in seismic activity across our study area. Most of the patterns we observe are also visible in event locations from earlier studies (e.g. Cahill and Isacks, 1992; Hayes et al., 2012) and global catalogs (e.g. International Seismological Center (ISC) and Advanced National Seismic System (ANSS)) but have not previously been discussed in any detail. While many of these patterns are difficult to explain, we propose that one in particular may provide clues into processes involved in the genesis of intermediate depth earthquakes. Specifically, along the projected location of the Nazca Ridge, we observe a marked gap in seismicity within the flat slab (shaded rectangle in Fig. 2b and dotted ellipse in Fig. 5b). The correlation between this gap in seismicity and the projected location of the Nazca Ridge has previously been noted (Hampel, 2002), but no explanation for the cause of this correlation has been presented. Given that other factors such as temperature, plate age, and pressure do not vary over these small length scales, one possible explanation for this change in seismicity could be related to differences in crustal thickness of the downgoing plate and the causes of intermediate depth seismicity.

While the causes of intermediate depth seismicity remain a subject of ongoing research, dehydration embrittlement could play a significant role in the genesis of these events in subduction zones worldwide. As the oceanic plate starts to subduct, it undergoes significant bending seaward of the trench axis and produce outer rise normal faults (Peacock, 2001). Previous studies have found evidence for seawater infiltration through these outer rise faults (Hussong et al., 1988). This seawater infiltration results in the formation of hydrous minerals (e.g. lawsonite, chlorite, and amphibole in the crust; serpentinite and talc in the mantle) along these fault planes to depths of 15–20 km or more (Peacock, 2001; Ranero et al., 2003). The breakdown of hydrous minerals at appropriate P–T conditions can lead to increases in pore pressure that decrease hydrostatic pressure and hence promote brittle failure required for intermediate depth seismicity (Raleigh and Paterson, 1965).

The Nazca Ridge has abnormally thick crust (~ 17 km) compared to the normal ~ 7 km thick oceanic crust on either side of it (Hampel et al., 2004). This additional crustal thickness results in 1.5 km of seafloor topography, but does not appear to affect patterns of outer rise faulting (Hampel et al., 2004). We propose that the crust along the Nazca Ridge is thicker than the penetration depth of water into the outer rise faults in this area. This would mean that only the oceanic crust (not the oceanic mantle lithosphere) is hydrated along the Nazca Ridge, resulting in an absence

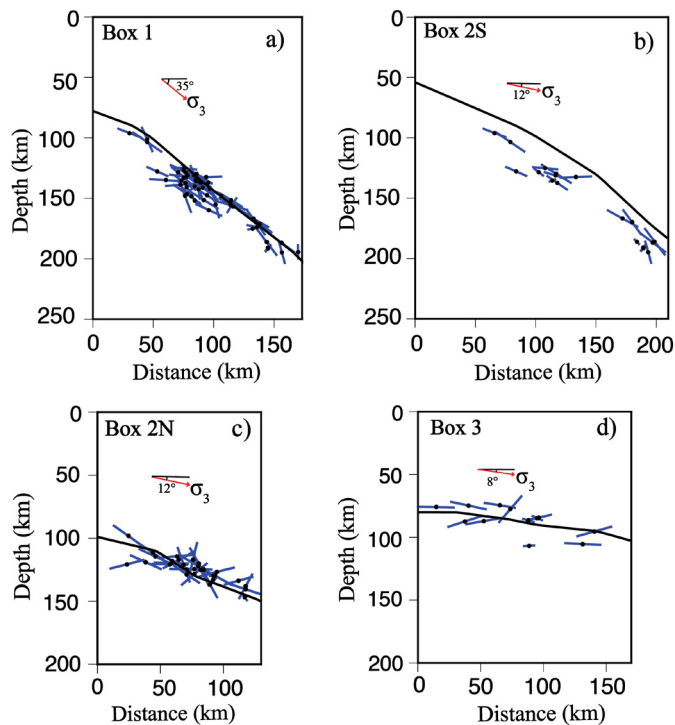


Fig. 10. (a–d) Cross sections showing the orientation of least compressive stress (red arrow) and T-axis vectors (small blue sticks) for four black rectangular regions inside Box 1, 2 (2S and 2N), and 3, respectively, shown in Fig. 8. Location of each cross section is shown as red diagonal line in the boxes shown in Fig. 8. Each cross section is oriented parallel to the average dip direction of the slab. The solid black line in each cross section is the slab contour from Antonijevic et al. (2015). T-axis vectors within each black rectangle are projected onto each cross-section. (For interpretation of the references to color in this figure legend, the reader is referred to the web version of this article.)

of typical mantle hydrous phases (e.g. serpentinite, talc). In contrast, the outer rise faults in the normal oceanic plate on either side of the ridge would contain both crustal and upper mantle hydrous phases. Seismicity up to ~ 80 km depth, close to the trench, is relatively continuously distributed along strike (Fig. 2a). A small break in seismic continuity (trenchward edge of cluster B, Fig. 2b), just south of the ridge projection, is due to the loss of events after relative relocation. We hypothesize that this along strike continuity in seismicity, up-dip from the horizontal portion of the flat slab, is related to the dehydration of hydrous minerals in the oceanic crust both within the ridge and in the normal crust on either side. We further propose that when the slab reaches 80 km depth, the crust is either dehydrated or the remaining hydrous phases are stable at the existing P/T conditions along the flat slab and therefore do not produce sufficient pore pressure to induce seismicity. Earthquakes that do occur north and south of the ridge along the flat portion of the slab are then caused by the dehydration of hydrated mantle lithosphere, not crust.

These dehydration reactions in the oceanic crust and uppermost mantle of the subducting plate are mainly temperature dependent (Babeyko and Sobolev, 2008). In the flat slab region, thermal structure of the subduction zone is affected by the timing of slab flattening (English et al., 2003), as the overriding plate in a flat subduction zone is no longer in contact with asthenospheric upper mantle. For similar subduction parameters (plate age, convergence velocity, etc.), a relatively older flat slab will therefore tend to have colder thermal structure than a slab region that has recently flattened. In southern Peru, the slab flattening event is fairly recent (~ 4 Ma ago; Rosenbaum et al., 2005) at the current location of ridge subduction ($\sim 15^\circ$ S), making steady state thermal models (e.g. English et al., 2003) inappropriate for this area. The existing

dynamic model (Manea et al., 2011) for the thermal structure of the Chilean flat slab, which experienced flattening for a comparatively longer period of time (~ 8.6 Ma; Ramos et al., 2002), may not be completely applicable for southern Peru. Further work to better constrain the likely temperatures across the Peruvian flat slab and the effect of these temperatures on dehydration reactions are needed to test these hypotheses and better understand the unusual patterns of observed seismicity across the subducted Nazca Ridge.

The triangular seismic gap (shaded triangle, Fig. 2b) observed between cluster A and B is also noticeable in the previous studies (Cahill and Isacks, 1992), but never reported explicitly. Because we note an excellent spatial correlation between the subducting Nazca Ridge (bathymetric feature) and seismic gap along the projected continuation of the ridge, we looked for evidence of any equivalent subducting bathymetric feature that can be correlated to this triangular seismic gap. One such bathymetric feature is the Nazca Fracture Zone, a narrow (25–50 km wide) oceanic fracture zone immediately south of the Nazca Ridge (Robinson et al., 2006), which is currently subducting along the northern edge of this triangular seismic gap (Fig. 1). The projected location of this ridge would likely be located near the northernmost corner of this gap, making its association with this absence of seismicity difficult to explain. Another bathymetric feature located further to the south is Iquique Ridge (Fig. 1). Kinematic reconstructions (Rosenbaum et al., 2005) suggest that the subduction of Iquique ridge started very recently (< 2 Ma). It is therefore unlikely that this ridge has reached a sufficient depth to affect the seismicity in this area. It is possible that our observed gap in seismicity is related to an unknown, fully subducted heterogeneity in the subducting plate, but we are unable to image any such structure at this time.

5.2. State of stress of the Nazca slab

We have analyzed the state of stress for the Nazca slab south of the Nazca ridge where the plate undergoes a dramatic change in dip angle. Recent studies have shown that this transition in slab dip is accommodated not by a tear, but by along-strike stretching of the Nazca plate (Phillips and Clayton, 2014). This extension is pervasive enough to have altered the fabric of the downgoing slab (Eakin et al., 2016).

We observe some variability in the T-axis orientations relative to the downdip direction (Fig. 9), but our stress tensor orientations show that the slab is experiencing down-dip extension in all four areas in which we had sufficient data to calculate the regional stress field (Figs. 8 and 9). Differences between T-axis orientations and slab dip vectors are observed in other subduction zones (Anderson et al., 2007) and could be related to strain partitioning along preexisting planes of weaknesses that are variably oriented with respect to the downdip direction. The regional stress field is more reliable indicator of ambient stress (Angelier et al., 1982). We note that the azimuth of the downdip direction varies from NNE to SW, but the σ_3 axis is always parallel to the slab surface, and in the downdip direction (Fig. 10). The only minor exception is a subtle clockwise rotation in the southernmost segments of the normally dipping slab (Fig. 9a). This rotation in σ_3 axis is perhaps an effect of the trench's stress state further south, where the strike of the trench rotates clockwise from NW–SE to N–S. Previously, Brudzinski and Chen (2005) found the T-axes to be dominantly oriented east–west (perpendicular to the trench) at $\sim 22^\circ$ S, just south of our study area. It is possible that the close proximity with the due eastward subducting slab to the south is affecting the state of stress in our southernmost regions. Downdip extension is seen in a number of subduction zones globally (e.g. Isacks and Molnar, 1971; Delouis et al., 1996; Wada et al., 2010), especially at depths of > 50 km (Anderson et al., 2007; Rontogianni et al., 2011). This

is thought to be due to slab pull, a dominant driving force for plate subduction (Forsyth and Uyeda, 1975).

While the direction of maximum extension is uniformly downdip, there is an alternating pattern in the direction of maximum compression (σ_1) from south to north. In Box 1 and Box 2N (Fig. 9a and c), maximum compression is oriented nearly horizontally, parallel to the slab surface in the along-strike direction of the slab (i.e. orthogonal to the downdip direction). In Box 2S and Box 3 (Fig. 9b and d), the maximum compressive stress is orthogonal to the slab surface. This variability in the direction of maximum compression is seen in other subduction zones (e.g. Bohnhoff et al., 2005; Rontogianni et al., 2011), and may be attributable to forces associated with the along-strike bending and unbending of the slab (“table-cloth effect”) (Creager et al., 1995). The exact patterns of along strike compression or (relative) extension will depend on the depth of the earthquakes relative to the slab surface, and the precise geometry of the slab over relatively small spatial scales. More data would be needed for this level of detail, and would be helpful for future modeling studies.

6. Conclusions

We use new data collected as part of three separate but temporally and spatially overlapping deployments to study the WBZ seismicity and state of stress of the Nazca plate underneath central and southern Peru. We observe a marked absence of seismicity along the projected location of the subducting Nazca ridge track. This observed variation in seismicity is likely related to the over-thickened crust (~ 17 km) of the Nazca Ridge, compared to the normal oceanic crust on either side of the ridge. It is possible that the depth of hydration of the outer rise faults along the Nazca Ridge is less than the crustal thickness of the ridge, which would imply that only the crust along the ridge is hydrated and the underlying mantle lithosphere is dry. In contrast, the outer rise faults in the normal oceanic slab on either side of the ridge would contain both the crust and upper mantle hydrous phases. We hypothesize that the along strike continuity in seismicity up to ~ 80 km depth is related to the dehydration of crustal hydrous phases both along the ridge as well as north and south of the ridge. Earthquakes that do occur north and south of the ridge, beyond 80 km depth, are likely due to the dehydration of hydrated mantle lithosphere at these locations. The current state of stress in the Nazca slab south of the Nazca Ridge suggests a dominant effect of slab pull acting in the downdip direction. The along strike variation in the orientation of maximum compressive stress is likely related to bending or unbending of the slab due to changes in the slab's curvature.

Acknowledgements

We are thankful to the Incorporated Research Institutions for Seismology (IRIS) and personnel at the PASSCAL Instrument Center for their help and support throughout the CAUGHT and PULSE deployment. The seismic instruments were provided by UNC-Chapel Hill, Yale University, and IRIS through the PASSCAL Instrument Center. This work was supported by National Science Foundation awards EAR-0908777, EAR-0907880, EAR-0944184, EAR-0943991, and EAR-0943962. We are thankful to Rob Clayton and Paul Davis for sharing data from 8 stations of the PERUSE network. We sincerely thank C. Condori Quispe and the staff at the Instituto Geofísico del Perú, Lima, Peru, and the staff at the San Calixto Observatory in Bolivia for their help and logistical support in deployment and demobilization efforts, as well as Mike Fort (PASSCAL) for his invaluable assistance in the field. Special thanks to C. Berk Biryol and S. Knezevic Antonijevic for helpful discussions. Maps

were created using the Generic Mapping Tools (GMT) software (Wessel and Smith, 1991).

Appendix A. Supplementary material

Supplementary material related to this article can be found online at <http://dx.doi.org/10.1016/j.epsl.2016.02.023>.

References

- Aki, K., Lee, W.H.K., 1976. Determination of three-dimensional velocity anomalies under a seismic array using first P arrival times from local earthquakes: 1. A homogeneous initial model. *J. Geophys. Res.* 81, 4381–4399. <http://dx.doi.org/10.1029/JB081i023p04381>.
- Anderson, M., Alvarado, P., Zandt, G., Beck, S., 2007. Geometry and brittle deformation of the subducting Nazca Plate, Central Chile and Argentina. *Geophys. J. Int.* 171, 419–434. <http://dx.doi.org/10.1111/j.1365-246X.2007.03483.x>.
- Angelier, J., Tarantola, A., Valette, B., Manoussis, S., 1982. Inversion of field data in fault tectonics to obtain the regional stress, I. Single phase fault populations, a new method of computing the stress tensor. *Geophys. J. Int.* 69, 607–621. <http://dx.doi.org/10.1111/j.1365-246X.1982.tb02766>.
- Antonijevic, S.K., Wagner, L.S., Kumar, A., Beck, S.L., Long, M.D., Zandt, G., Tavera, H., Condori, C., 2015. The role of ridges in the formation and longevity of flat slabs. *Nature* 524 (7564), 212–215. <http://dx.doi.org/10.1038/nature14648>.
- Babeyko, A.Y., Sobolev, S.V., 2008. High-resolution numerical modelling of stress distribution in visco-elasto-plastic subducting slabs. *Lithos* 103, 1–2. <http://dx.doi.org/10.1016/j.lithos.2007.09.015>.
- Bishop, B., Beck, S.L., Zandt, G., Scire, A., Wagner, L.S., Long, M.D., Tavera, H., 2014. Peruvian trench to Andean thrust front: evidence for coupling of the Peruvian flat slab to the over-riding South American Plate. In: *AGU Fall Meeting*. San Francisco, California.
- Bissig, T., Ullrich, T.D., Tosdal, R.M., Friedman, R., Ebert, S., 2008. The time–space distribution of Eocene to Miocene magmatism in the central Peruvian polymetallic province and its metallogenetic implications. *J. South Am. Earth Sci.* 26, 16–35. <http://dx.doi.org/10.1016/j.jsames.2008.03.004>.
- Bohnhoff, M., Harjes, H.P., Meier, T., 2005. Deformation and stress regimes in the Hellenic subduction zone from focal mechanisms. *J. Seismol.* 9, 341–366.
- Boyd, T.M., Snoko, J.A., Sacks, I.S., Rodriguez, A., 1984. High-resolution determination of the Benioff zone geometry beneath southern Peru. *Bull. Seismol. Soc. Am.* 74, 559–568.
- Brudzinski, M.R., Chen, W.-P., 2005. Earthquakes and strain in subhorizontal slabs. *J. Geophys. Res.* 110, B08303. <http://dx.doi.org/10.1029/2004JB003470>.
- Cahill, T., Isacks, B.L., 1992. Seismicity and shape of the subducted Nazca plate. *J. Geophys. Res.* 97, 17,503–17,529. <http://dx.doi.org/10.1029/92JB00493>.
- Creager, K.C., Chiao, L.-Y., Winchester, J.P., Engdahl, E.R., 1995. Membrane strain rates in the subducting plate beneath, South America. *Geophys. Res. Lett.* 22, 2321–2324. <http://dx.doi.org/10.1029/95GL02321>.
- Delouis, B., Cisternas, A., Dorbath, L., Rivera, L., Kausel, E., 1996. The Andean subduction zone between 22° and 25°S (northern Chile): precise geometry and state of stress. *Tectonophysics* 259, 81–100. [http://dx.doi.org/10.1016/0040-195\(95\)00065-8](http://dx.doi.org/10.1016/0040-195(95)00065-8).
- Delvaux, D., Sperner, B., 2003. Stress tensor inversion from fault kinematic indicators and focal mechanism data: the TENSOR program. In: *Nieuwland, D. (Ed.), New Insights into Structural Interpretation and Modelling*. Geol. Soc. (Lond.) Spec. Publ. 212, 75–100.
- Dickinson, W., Snyder, W.S., 1978. Plate tectonics of the Laramide orogeny. In: *Geol. Soc. Am. Mem.*, vol. 151, pp. 355–366.
- Dorbath, C., Granet, M., 1996. Local earthquake tomography of the Altiplano and Eastern Cordillera of northern Bolivia. *Tectonophysics* 259, 117–136. [http://dx.doi.org/10.1016/0040-1951\(95\)00052-6](http://dx.doi.org/10.1016/0040-1951(95)00052-6).
- Dougherty, S.L., Clayton, R.W., 2014. Seismic structure in southern Peru: evidence for a smooth contortion between flat and normal subduction of the Nazca Plate. *Geophys. J. Int.* 200, 534–555. <http://dx.doi.org/10.1093/gji/ggu415>.
- Eakin, C.M., Maureen, M.D., Scire, A., Beck, S.L., Wagner, L.S., Zandt, G., Tavera, H., 2016. Internal deformation of the subducted Nazca slab inferred from seismic anisotropy. *Nat. Geosci.* 9, 56–60. <http://dx.doi.org/10.1038/NGEO2592>.
- English, J.M., Johnston, S.T., Wang, K., 2003. Thermal modelling of the Laramide Orogeny: testing the flat-slab subduction hypothesis. *Earth Planet. Sci. Lett.* 214, 619–632. [http://dx.doi.org/10.1016/S0012-821X\(03\)00399-6](http://dx.doi.org/10.1016/S0012-821X(03)00399-6).
- Forsyth, D., Uyeda, S., 1975. On the relative importance of the driving forces of plate motion. *Geophys. J. R. Astron. Soc.* 43, 163–200. <http://dx.doi.org/10.1111/j.1365-246X.1975.tb00631>.
- Gerya, T.V., Fossati, D., Cantieni, C., Seward, D., 2009. Dynamic effects of aseismic ridge subduction: numerical modelling. *Eur. J. Mineral.* 21, 649–661. <http://dx.doi.org/10.1127/0935-1221/2009/0021-1931>.
- Gripp, A.E., Gordon, R.J., 2002. Young tracks of hotspots and current plate velocities. *Geophys. J. Int.* 150, 321–361. <http://dx.doi.org/10.1046/j.1365-246X.2002.01627.x>.

- Hampel, A., 2002. The migration history of the Nazca Ridge along the Peruvian active margin: a re-evaluation. *Earth Planet. Sci. Lett.* 203, 665–679. [http://dx.doi.org/10.1016/S0012-821X\(02\)00859-2](http://dx.doi.org/10.1016/S0012-821X(02)00859-2).
- Hampel, A., Kukowski, N., Bialas, J., Huebscher, C., Heinbockel, R., 2004. Ridge subduction at an erosive margin: the collision zone of the Nazca Ridge in southern Peru. *J. Geophys. Res.* 109 (2). <http://dx.doi.org/10.1029/2003JB002593>.
- Hasegawa, A., Sacks, I.S., 1981. Subduction of the Nazca Plate beneath Peru as determined from seismic observations. *J. Geophys. Res.* 86, 4971–4980. <http://dx.doi.org/10.1029/JB086iB06p04971>.
- Havskov, J., Ottmoller, L., 1999. SeisAn earthquake analysis software. *Seismol. Res. Lett.* 70, 532–534. <http://dx.doi.org/10.1785/gssrl.70.5.532>.
- Hayes, G.P., Wald, D.J., Johnson, R.L., 2012. Slab1.0: a new three-dimensional model of global subduction interface geometry. *J. Geophys. Res.* 117, B01302. <http://dx.doi.org/10.1029/2011JB008524>.
- Henry, S.G., Pollack, H.N., 1988. Terrestrial heat flow above the Andean subduction zone in Bolivia and Peru. *J. Geophys. Res.* 93, 15,153–15,162. <http://dx.doi.org/10.1029/JB093iB12p15153>.
- Hu, J., Liu, L., Hermsillo, A., Zhou, Q., 2016. Simulation of late Cenozoic South American flat-slab subduction using geodynamic models with data assimilation. *Earth Planet. Sci. Lett.* 438. <http://dx.doi.org/10.1016/j.epsl.2016.01.011>.
- Humphreys, E., Hessler, E., Dueker, K., Farmer, G.L., Erslev, E., Atwater, T., 2003. How laramide-age hydration of North American Lithosphere by the Farallon Slab controlled subsequent activity in the Western United States. *Int. Geol. Rev.* 45 (7), 575–595. <http://dx.doi.org/10.2747/0020-6814.45.7.575>.
- Hussong, D.M., Reed, T.B., Bartlett, W.A., 1988. SEA-MARC II sonar imagery and bathymetry of the Nazca plate and forearc, ODP Leg 112. In: Suess, E., von Huene, R., et al. (Eds.), *Proceedings of the Ocean Drilling Program, Scientific Results*, vol. 112. Ocean Drilling Program, College Station, Texas, pp. 125–130.
- Isacks, B.L., Barazangi, M., 1977. Geometry of Benioff zones: lateral segmentation and downwards bending of the subducted lithosphere. In: Talwani, M., Pitman, W.C. (Eds.), *Island Arcs, Deep Sea Trenches and Backarc Basins*. American Geophysical Union, Washington, pp. 99–114.
- Isacks, B., Molnar, P., 1971. Distribution of stresses in the descending lithosphere from a global survey of focal-mechanism solutions of mantle earthquakes. *Rev. Geophys.* 9, 103–174. <http://dx.doi.org/10.1029/RG009i001p0103>.
- Jordan, T.E., Allmendinger, R.W., 1986. The Sierras Pampeanas of Argentina: a modern analogue of Rocky Mountain foreland deformation. *Am. J. Sci.* 286, 737–764.
- Manea, V.C., Gurnis, M., 2007. Subduction zone evolution and low viscosity wedges and channels. *Earth Planet. Sci. Lett.* 264 (1–2), 22–45. <http://dx.doi.org/10.1016/j.epsl.2007.08.030>.
- Manea, V.C., Pérez-Gussinyé, Marta, Manea, M., 2011. Chilean flat slab subduction controlled by overriding plate thickness and trench rollback. *Geology* 40, 35–38. <http://dx.doi.org/10.1130/G32543.1>.
- Marot, M., Monfret, T., Pardo, M., Ranalli, G., Nolet, G., 2013. A double seismic zone in the subducting Juan Fernandez Ridge of the Nazca Plate (32°S) central Chile. *J. Geophys. Res.* 118, 3462–3475. <http://dx.doi.org/10.1002/jgrb.50240>.
- Peacock, S.M., 2001. Are the lower planes of double seismic zones caused by serpentine dehydration in subducting oceanic mantle? *Geology* 29, 299–302. [http://dx.doi.org/10.1130/0091-7613\(2001\)029](http://dx.doi.org/10.1130/0091-7613(2001)029).
- Phillips, K., Clayton, R.W., 2014. Structure of the subduction transition region from seismic array data in southern Peru. *Geophys. J. Int.* 196, 1889–1905. <http://dx.doi.org/10.1093/gji/ggt504>.
- Raleigh, C.B., Paterson, M.S., 1965. Experimental deformation of serpentinite and its tectonic implications. *J. Geophys. Res.* 70, 3965–3985. <http://dx.doi.org/10.1029/JZ070i016p03965>.
- Ramos, V.A., Cristallini, E., Perez, D.J., 2002. The Pampean flat-slab of the Central Andes. *J. South Am. Earth Sci.* 15, 59–78. [http://dx.doi.org/10.1016/S0895-9811\(02\)00006-8](http://dx.doi.org/10.1016/S0895-9811(02)00006-8).
- Ranero, C.R., Phipps Morgan, J., McIntosh, K., Reichert, C., 2003. Bending-related faulting and mantle serpentinization at the Middle America trench. *Nature* 425, 367–373. <http://dx.doi.org/10.1038/nature01961>.
- Reasenber, P., Oppenheimer, D., 1985. FPFIT, FPLOT and FPPAGE: FORTRAN computer programs for calculating and displaying earthquake fault-plane solutions. In: *USGS Open File Rept.*, pp. 85–739.
- Robinson, D.P., Das, S., Watts, A., 2006. Earthquake rupture stalled by a subducting fracture zone. *Science* 312, 1203–1205. <http://dx.doi.org/10.1126/science.1125771>.
- Rontogianni, S., Konstantinou, K.I., Melis, N.S., Evangelidis, C.P., 2011. Slab stress field in the Hellenic subduction zone as inferred from intermediate depth earthquakes. *Earth Planets Space* 63, 139–144. <http://dx.doi.org/10.5047/eps.2010.11.011>.
- Rosenbaum, G., Giles, D., Saxon, M., Betts, P.G., Weinberg, R.F., Duboz, C., 2005. Subduction of the Nazca Ridge and the Inca Plateau: insights into the formation of ore deposits in Peru. *Earth Planet. Sci. Lett.* 239, 18–32. <http://dx.doi.org/10.1016/j.epsl.2005.08.003>.
- Skinner, S.M., Clayton, R.W., 2013. The lack of correlation between flat slabs and bathymetric impactors in South America. *Earth Planet. Sci. Lett.* 371–372, 1–5. <http://dx.doi.org/10.1016/j.epsl.2013.04.013>.
- Wada, I., Mazzotti, S., Wang, K., 2010. Intraslab stresses in the Cascadia subduction zone from inversion of earthquake focal mechanisms. *Bull. Seismol. Soc. Am.* 100, 2002–2013. <http://dx.doi.org/10.1785/0120090349>.
- Waldhauser, F., Ellsworth, W.L., 2000. A double-difference earthquake location algorithm: Method and application to the Northern Hayward Fault, California. *Bull. Seismol. Soc. Am.* 90, 1353–1368. <http://dx.doi.org/10.1785/0120000006>.
- Wessel, P., Smith, W.H.F., 1991. Free software helps map and display data. *Trans. Am. Geophys. Union* 72, 441–445. <http://dx.doi.org/10.1029/90EO00319>.